

Highly Efficient Metasurface Quarter-Wave Plate with Wave Front Engineering

Chen Chen, Shenglun Gao, Xingjian Xiao, Xin Ye, Shengjie Wu, Wange Song, Hanmeng Li, Shining Zhu, and Tao Li*

Metasurfaces with local phase tuning by subwavelength elements promise unprecedented possibilities for ultrathin and multifunctional optical devices in which geometric phase design is widely used due to its resonant-free and large tolerance in fabrications. By arranging the orientations of anisotropic nanoantennas, the geometric phase-based metasurfaces can convert the incident spin light to its orthogonal state, and enable flexible wave front engineering together with the function of a half-wave plate. Herein, by incorporating the propagation phase, another important optical device of quarter-wave plate together with the wave front engineering as well, which is implemented by controlling both the cross- and copolarized light simultaneously with a singlet metasurface, is realized. Highly efficient conversion of the spin light to a variety of linearly polarized light is obtained for meta-holograms, metalens focusing and imaging in the blue light region. This work provides a new strategy for efficient metasurfaces with both phase and polarization control, and enriches the functionalities of metasurface devices for wider application scenarios.

1. Introduction

The emergence of metasurfaces with ultrathin, ultralight, and multifunctional advantages has spurred significant interest in light manipulations.^[1–7] By judiciously designing the field discontinuities across the interface with different meta-atoms, full control of sophisticated wave fronts, polarization states, and their energy allocations can be achieved.^[8–10] Plentiful functionalities with great potential in applications are demonstrated, such as


metalens,^[11–15] metaholograms,^[16–18] and polarizers,^[19–21] to name a few. Among them, simultaneous control of the polarization and phase plays a vital role and has already aroused numerous researches to explore its full potential.^[22–26] Attempts such as utilizing two plasmonic nanopillars per period with different distance and orientation angle only work for oblique incidence.^[27] Another method is exploiting the superposition of the two output circular polarization (CP) beams through two sets of nanopillars with different dimensions and starting orientation angles under linear polarization (LP) incidence.^[28] Both of them are based on super unit cells with spatial superposition of inclusions, which would result in lower efficiency, inferior image quality, and lower space-bandwidth product. Recently, it is of great interest to combine the propagation phase and geometric phase (i.e., Pancharatnam–Berry [PB] phase) to realize full control of the polarization and phase on a single subwavelength unit cell.^[29–35]

However, they are usually focused on the polarization multiplexing to enhance the information capability, e.g., different functionalities are encoded with different polarization states. In fact, incorporating the same wave front engineering with different polarization states to realize specific polarization conversion is quite useful but remains rarely explored. As a basic optical component, quarter-wave plate (QWP) (normally convert the CP light to LP light and vice versa) plays an important role in light manipulation.^[36,37] It would be highly desirable to find ways to implement QWPs on a single metasurface.

Here, we provide a straightforward design principle for metasurfaces (e.g. metaholograms and metalens) to achieve the QWP functionality by utilizing both the copolarized and cross-polarized spin light. By combining the propagation phase with PB phase, we first demonstrate the modulate capacity with spin-selected holographic images (the commonly unmodulated copolarized light and cross-polarized light) with SiNx metasurfaces in the visible spectrum. We further realize the QWPs with wave manipulation abilities by controlling the superposition of two output CP light. Other elliptical polarizations with designed wave front are also produced experimentally. The polarization reconstruction and wave manipulation based on two orthogonal CP bases certainly expands the practical application possibilities and can trigger versatile function integrations for advanced compact systems.

C. Chen, S. Gao, X. Xiao, X. Ye, S. Wu, W. Song, H. Li, Prof. S. Zhu, Dr. T. Li
National Laboratory of Solid State Microstructures
Key Laboratory of Intelligent Optical Sensing and Manipulation
Jiangsu Key Laboratory of Artificial Functional Materials
College of Engineering and Applied Sciences
Nanjing University
Nanjing 210093, China
E-mail: taoli@nju.edu.cn

C. Chen, S. Gao, X. Xiao, X. Ye, S. Wu, W. Song, H. Li, Prof. S. Zhu, Dr. T. Li
Collaborative Innovation Center of Advanced Microstructures
Nanjing 210093, China

 The ORCID identification number(s) for the author(s) of this article can be found under <https://doi.org/10.1002/adpr.202000154>.

© 2020 The Authors. Advanced Photonics Research published by Wiley-VCH GmbH. This is an open access article under the terms of the Creative Commons Attribution License, which permits use, distribution and reproduction in any medium, provided the original work is properly cited.

DOI: 10.1002/adpr.202000154

2. The Design Principles

PB phase-based metasurfaces can achieve a full phase control by adjusting the orientation angle of the meta-atoms with identical geometry.^[38] The cross-polarized light will have extra $\mp 2\sigma\theta$ phase modulation under normal CP light incidence, where θ is the rotation angle from the x -axis, and σ indicates the handedness of the CP light. However, the copolarized scattered light is usually ignored, which unavoidably results in background noises or a dazzling spot in the hologram image.^[28,31,39,40] To surmount this restriction, we propose to modulate the copolarized and cross-polarized light independently by combining the propagation phase and PB phase. The total Jones matrix describing the relation between the input electric field (E_{in}) and the output electric field (E_{out}) in a circular base can be written as

$$J = R_c(-\theta) \begin{bmatrix} e^{i\phi_{RR}} & e^{i\phi_{RL}} \\ e^{i\phi_{LR}} & e^{i\phi_{LL}} \end{bmatrix} R_c(\theta) = \begin{bmatrix} e^{i\phi_{RR}} & e^{i(2\theta+\phi_{RL})} \\ e^{i(-2\theta+\phi_{LR})} & e^{i\phi_{LL}} \end{bmatrix} \quad (1)$$

where $R_c(\theta)$ is the rotation matrix, ϕ_{RL} , ϕ_{LR} , ϕ_{RR} , and ϕ_{LL} are the propagation phases. In this work, we consider the widely used rectangular nanopillars, so the phase shift $\phi_{RR} = \phi_{LL}$ and $\phi_{RL} = \phi_{LR}$ due to the mirror symmetry. In this case, if the incident wave is right circularly polarized (RCP), the output electric field E_{out} becomes

$$E_{out} = JE_{in} = \begin{bmatrix} e^{i\phi_{RR}} & e^{i(2\theta+\phi_{RL})} \\ e^{i(-2\theta+\phi_{LR})} & e^{i\phi_{RR}} \end{bmatrix} \begin{bmatrix} 1 \\ 0 \end{bmatrix} = \begin{bmatrix} e^{i\phi_{RR}} \\ e^{i(-2\theta+\phi_{RL})} \end{bmatrix} \quad (2)$$

From Equation (2), we can clearly conduct the phase modulation for the transmitted/reflected RCP and LCP wave independently. For example, if the transmitted/reflected RCP light is designed for a special function with the phase profile $\varphi_1(x,y)$ and the LCP light with another phase profile $\varphi_2(x,y)$, then $\varphi_1(x,y) = \phi_{RR}(x,y)$, and $\varphi_2(x,y) = -2\theta(x,y) + \phi_{RL}(x,y)$. It means the phase manipulation can be implemented by arranging different nanopillars with different rotation angles in different positions. Moreover, if a reference phase ($\varphi = -2\theta_0$) is added to $\varphi_2(x,y)$, representing all the nanopillars rotating θ_0 extra angle, which does not influence the wave manipulation capacity, but it surely affects the output polarization state considering the superposition of the other CP light. The schematics of the electric field changing process (RCP beam $|R\rangle$ passing through a rotated nanopillar) is shown in **Figure 1a**, the output two beams can be written as $a_R e^{i\phi_{RR}} |R\rangle$ and $a_L e^{i(\phi_{RL}-2\theta-2\theta_0)} |L\rangle$, where a_R and a_L are the corresponding amplitudes of the output RCP and LCP beams. Ignoring the material loss, the amplitude distributions of the two output CP light are shown in **Figure 1c**, relevant to the specific structure parameters and complementary to each other. The aforementioned reference phase φ is related to the total extra rotation angle θ_0 , with its relationship shown in **Figure 1d**. If the wave manipulations of the two CP light are the same with each other ($\phi_{RR} = \phi_{RL} - 2\theta$), then the superimposed

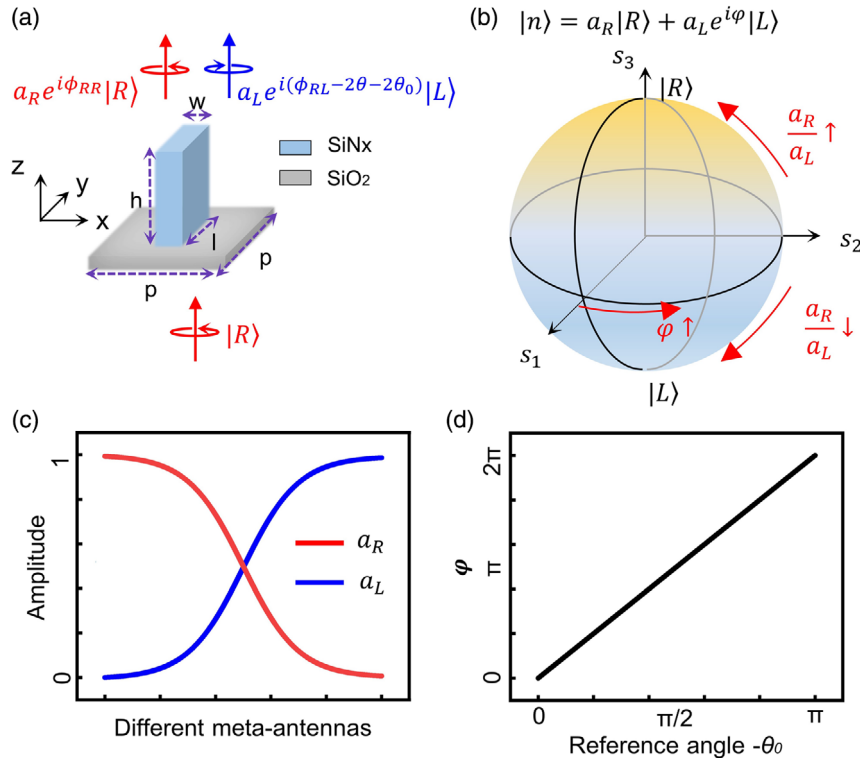


Figure 1. Schematics of the design principle. a) Electric field changing process through a dielectric rotated nanopillar. b) Poincaré sphere containing the full polarization states with different reference phase φ and amplitudes a_R and a_L . c) Amplitude distribution with different meta-antennas. d) Relationship of the reference phase φ added to LCP and the total extra rotation angle θ_0 .

polarization state can be written as $|n\rangle = a_R|R\rangle + a_L e^{i\varphi}|L\rangle$, where a_R/a_L and φ can be independently modulated. In this way, as shown in Figure 1b, an arbitrary polarization state can be reconstructed by changing a_R/a_L (shifting along the longitude direction) and φ (moving along latitude direction), covering the whole Poincaré sphere. The azimuth angle ψ and ellipticity angle χ can be derived as $\psi = \theta_0$ and $\chi = \frac{1}{2} \arcsin \frac{a_R^2 - a_L^2}{a_R^2 + a_L^2}$.

3. Experimental Results

3.1. Phase Modulation Capability

As a proof of concept, we consider the silicon nitride (SiN_x) metasurfaces consisting of nanopillars with different shapes covered on the fused-silica substrate. SiN_x was chosen because of its low loss in visible light and compatibility with complementary metal–oxide semiconductor (CMOS) processes. The design wavelength is 470 nm and the metasurface works in a transmitted way. As shown in Figure 1a, the unit cell period is chosen as 300 nm satisfying the Nyquist theory.^[41] The nanopillar height is set as 800 nm to provide phase change covering $0-2\pi$. Figure 2a shows the simulated efficiency distribution of nanopillars with different widths and lengths for the transmitted RCP and LCP light with RCP light incidence. The simulated phase responses of the nanopillars for the working RCP (ϕ_{RR}) and LCP (ϕ_{RL}) light are shown in Figure 2b,c, respectively. The purple dots mark the selected antennas with required phase responses and homogeneous amplitudes (to satisfy $a_R/a_L = 1$). The tolerance analysis of the antennas is shown in Figure S1, Supporting Information. Figure 2d shows the specific amplitude distribution, the average amplitude for RCP light is $a_R = 0.47$,

and for LCP light is $a_L = 0.46$, nearly equal to each other. It is worth mentioning that the propagation phase responses are limited when maintaining the high a_L (spin conversion efficiencies) requirements (see Figure S2, Supporting Information), which will deteriorate the performances in the circumstances such as the spin-decoupled wave front manipulation. Although utilization of the a_R , which reducing the high a_L limits and extending the propagation phase responses, fully exerts the superiorities of combining propagation phase and geometric phase.

To verify the phase modulation ability, we first demonstrated an independent spin polarization hologram metasurface with RCP light incidence. The transmitted RCP light was modulated to produce a far-field hologram image with “NJU” based on propagation phase (ϕ_{RR}) and LCP light is manipulated to present a representative building of Nanjing University (i.e., a 600 years building named Bei-Da) in the far-field based on propagation phase (ϕ_{RR}) and PB phase ($\phi_{RL} - 2\theta$). The optimized phase profiles are based on Gerchberg–Saxton algorithm.^[42–44] The metasurface with a footprint of $150 \mu\text{m} \times 150 \mu\text{m}$ is fabricated using a conventional nanofabrication process (see the Experimental Section) and its scanning electron microscopy (SEM) image is shown in Figure 2e. The experimental light intensity profiles for the transmitted RCP and LCP light in the projected plane are shown in Figure 2f, which are consistent with the designed images and have negligible zero spots.

3.2. Metaholograms with QWP Effect

After verifying the phase modulation capability, we further demonstrate the polarization state manipulation. The output RCP and LCP light are designed with the same function (e.g., the same focal length or the same hologram image) by modulating

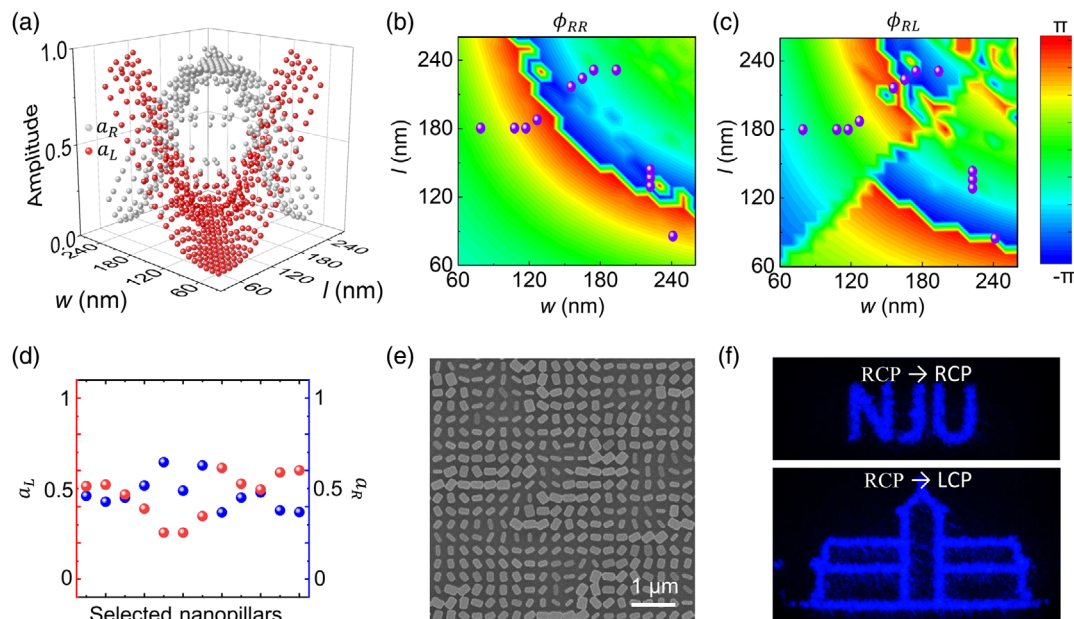


Figure 2. Independent wave manipulation of the two output CP beams. a) Simulated amplitude distribution of the transmitted RCP and LCP light with the nanopillar's geometric parameters under RCP incidence. Phase responses of the transmitted b) RCP and c) LCP light with different nanopillars under RCP incidence. Purple dots mark the chosen antennas. d) Amplitude distribution of the selected nanopillars. e) SEM image of the fabricated metasurface. f) Metahologram images with RCP and LCP analyzer.

the propagation phase $\phi_{RR}(x,y)$ and the compensatory PB phase $-2\theta(x,y)$. To realize the QWP functionality, we choose the same nanopillars as shown in Figure 2b to obtain equal a_R and a_L . The reference phase φ (related to the extra rotation angle θ_0) is modulated to get different LP light. As shown in Figure 3a, the red dots on the Poincaré sphere mark the designed output LP state under RCP incidence. The SEM image of the metasurface with a footprint of $150\ \mu\text{m} \times 150\ \mu\text{m}$ for x -polarized (dot A) hologram is shown in Figure 3b. The inset picture is the enlarged image. The directly (without analyzer) measured holographic image is shown in Figure 3c. Due to the utilization of both the copolarized and cross-polarized light, the middle zero spot is nearly negligible, indicating a very high diffraction efficiency (98%). The zero spot is difficult to completely disappear because of k -space imaging of the light passing through the gap between nanopillars. To verify its polarization properties, we add a polarizer to detect the relative intensity profile. When the polarizer is set as 0° (the transmission axis is parallel to the x -axis), the hologram intensity profile (see Figure 3d) is nearly the same as the measured image without analyzer (Figure 3c). When the polarizer is rotated as 45° and 90° , the intensity of the output hologram image change from attenuation to disappearance that surely verifies the LP (x -polarized) properties (see Figure 3e,f), indicating the functionality of QWP together with wave manipulation. With different designed reference phase φ (the total extra rotation angle θ_0),

other output LP states can also be produced. Figure 3g-i show the measurements (without analyzer) of the other meta-QWPs (RCP to B: 45° , C: 90° and D: -45° LP) for holographic imaging. The respective inset SEM image, compared to the inset one in Figure 3b, reveals the different extra rotation angle of the whole nanopillars. Thus, hologram images with different LP states under RCP incidence can be obtained by rotating the metasurface nanopillars.

3.3. Metalens with QWP Effect

To further demonstrate the manipulation capability, we design a meta-QWP for focusing and imaging. As shown in Figure 4a, the designed single-layer metasurface can act as a QWP and a lens at the same time. The phase profile follows^[45] $\varphi_1(x,y) = \varphi_2(x,y) = \frac{2\pi}{\lambda}(f - \sqrt{x^2 + y^2 + f^2})$, where the focal length $f = 100\ \mu\text{m}$. Figure 4b shows the SEM image of the fabricated metalens ($D = 150\ \mu\text{m}$, numerical aperture (NA) = 0.6) with x -polarization output under RCP incidence (the detailed analysis are shown in Figure S3, Supporting Information). As demonstrated earlier, other LP output can also be obtained as long as rotating the metasurface. The directly measured focus spot is shown in Figure 4c, with the full width at half maximum (FWHM) of 477 nm. The focusing efficiency (the ratio of the

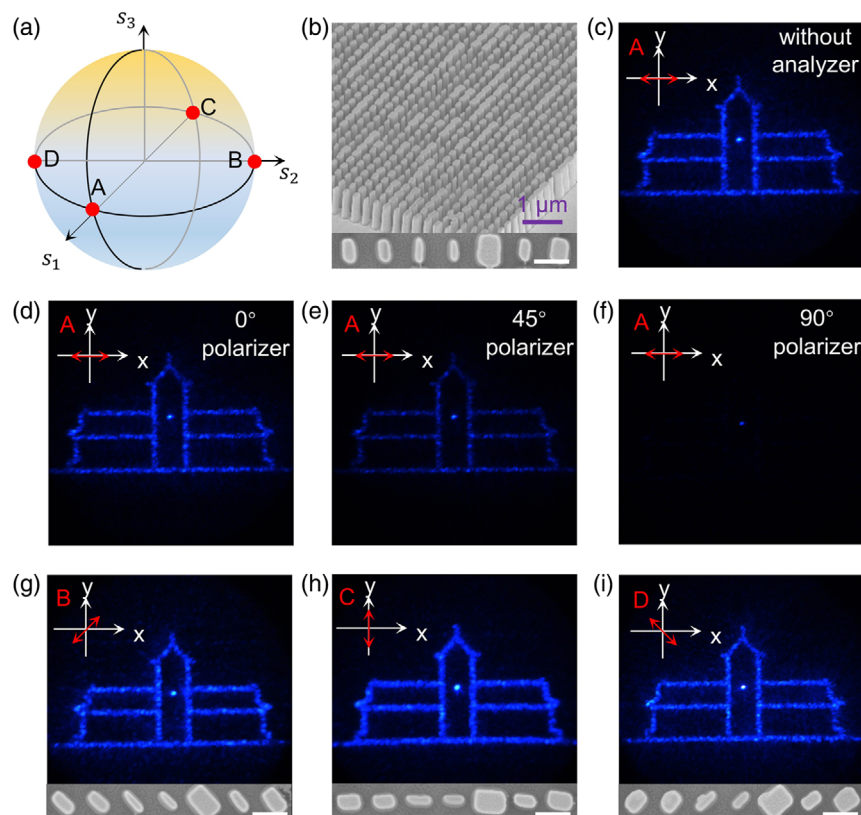


Figure 3. Different meta-QWPs for holographic imaging. a) Red dots on the Poincaré sphere indicate the designed output LP with RCP incidence. b) SEM images of the metasurface for x -polarized (A) output. Scale bar = 300 nm. c) Metahologram image (A: x -polarized) without analyzer. The intensity profiles of the hologram with a d) 0° polarizer, e) 45° polarizer, and f) 90° polarizer. Metahologram images without analyzer for g) B: 45° -polarization, h) B: 90° -polarization, and i) B: -45° -polarization. Insets are the corresponding SEM images. Scale bar = 300 nm.

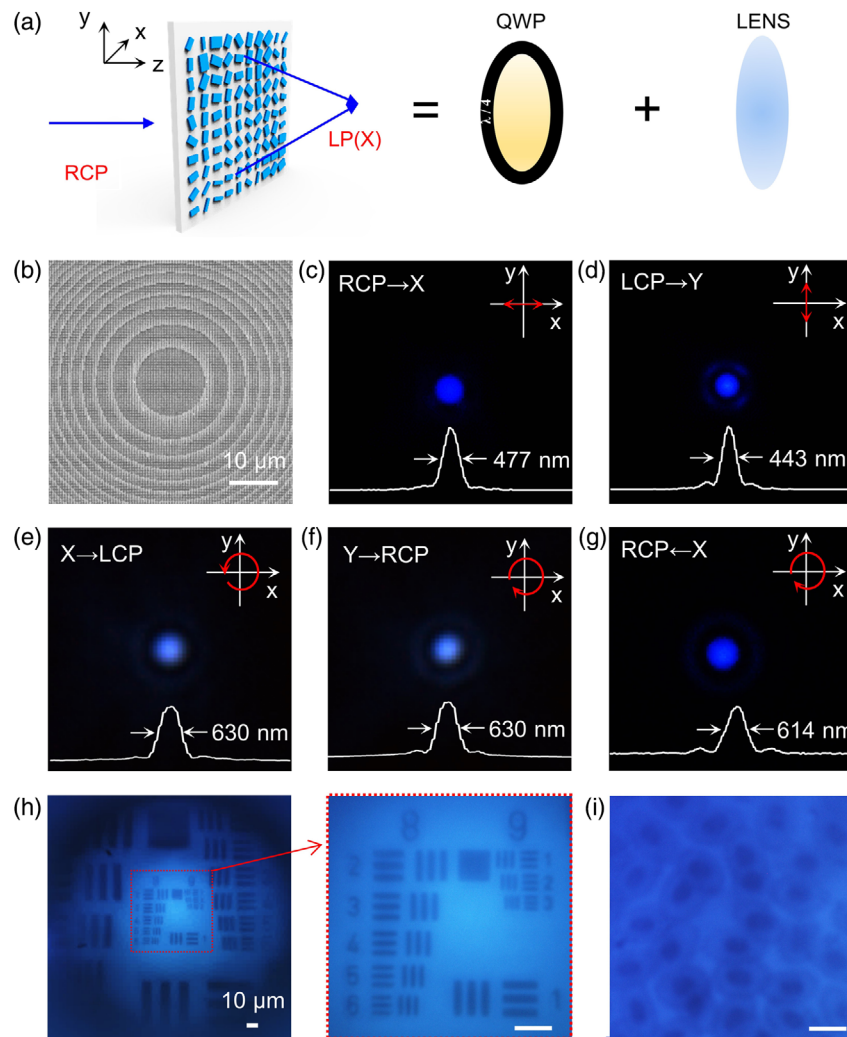


Figure 4. Meta-QWP for focusing and imaging. a) Schematic illustration of the metasurface acting as the QWP and the lens at the same time. b) SEM image of the fabricated metasurface. Intensity profiles of the focus when the incidence (from the substrate) is c) RCP, d) LCP, e) x -polarized, and f) y -polarized. The intensity profile of the focus when x -polarized light is incident from the side of the nanopillars. Images of the h) USAF resolution test chart and i) chicken erythrocytes (without analyzer) when directly illuminated by a halogen lamp with a filter of 470 nm. Scale bar = 10 μm .

optical power in an area of diameter $3 \times \text{FWHM}$ to the total transmitted power) is calculated as 53%. When incidence is switched to LCP light, the focus becomes y -polarized due to the superposition of the output LCP and RCP components, as shown in Figure 4d with FWHM of 443 nm. Similarly, when the illumination is x -polarized, the focus (FWHM is measured as 630 nm) is accordingly LCP (see Figure 4e), and the focus changes to RCP when the incidence is y -polarized (see Figure 4f) with the FWHM of 630 nm as well. If the front and back of the metasurface is flipped, the polarization changing rule will also be reversed accordingly. As shown in Figure 4g, when the x -polarized light is illuminated from the other side, the focus becomes RCP with the measured FWHM of 614 nm. The difference of FWHM in these situations is mainly due to the measurement error in the experiment. Here, simulations of the metalens with the same NA (0.6) are also performed to verify the focusing properties (Figure S4, Supporting Information). The simulated FWHM is 400 nm and the focusing

efficiency is 77%. The experimental quantitative results are not as good as the simulation ones due to the imperfections of the fabricated nanopillars. Yet, qualitative performances such as the polarization state properties are in high accordance with the simulations. Furthermore, we conduct the imaging test of the fabricated sample. The polarization of the image is consistent with the polarization of the focus. Figure S5, Supporting Information shows the image in the situation of Figure 4c (RCP incidence) without analyzer and with 90° polarizer, and the extinction properties indicate the x -polarization the image is. Note that the metasurface can also produce a good image regardless of the additional optical elements for generating and detecting the corresponding polarization, as shown in Figure 4h-i. The right side of the Figure 4h is the enlarged central part image of the 1951 United States Air Force (USAF) resolution test chart, manifesting clear resolution of Element 1 and Group 9 (i.e., a resolution of 980 nm). Figure 4i is the image of chicken erythrocytes, and the nuclei are clearly distinguishable.

3.4. Metalens with Elliptic Polarizations Generation

In addition, this method can be scaled to other polarization states, such as elliptic polarizations E and F on the Poincaré sphere (see Figure 5a). Specifically, for the polarization state E, $a_R/a_L = 1/2$ and $\varphi = 0$, the amplitude distribution of the selected nanopillars are shown in Figure 5b, with the average $a_R = 0.30$ and $a_L = 0.61$ ($a_R + a_L < 1$ is due to the intrinsic material loss), and the designed focal length is set as $200\ \mu\text{m}$ with $NA = 0.35$. Figure 5c shows the intensity profile of the focus with the FWHM of $1.18\ \mu\text{m}$ and the focusing efficiency of 81% (polarization analysis results are shown in Figure S6, Supporting Information). Figure 5d shows the image (without analyzers) of the ascaris eggs directly illuminated by a halogen lamp with a filter of $470\ \text{nm}$, clearly showing the elliptical shapes. Similarly, for the polarization state F, $a_R/a_L = 7/2$ and $\varphi = \pi$, and the corresponding amplitude distribution of the selected antennas are also shown in Figure 5e, with the average amplitude $a_R = 0.71$ and $a_L = 0.23$. The focal length is designed as $300\ \mu\text{m}$ with $NA = 0.24$. Enlarged focal spot with the FWHM of $1.60\ \mu\text{m}$ is shown in Figure 5f and the focusing efficiency is calculated as 87%. Figure 5g shows the image of Sector Star Target which resolution at the central circle is $8.7\ \mu\text{m}$. SEM images of these samples are shown in Figure S7, Supporting Information.

4. Conclusion

In conclusion, we have demonstrated a straightforward method for realizing phase manipulation and polarization control at the same time. Hologram images with negligible zero spots are obtained with high diffraction efficiencies (98%), and the LP properties are also verified. Metalens as a QWP is demonstrated experimentally as well. This method can be extended to acting as other wave plates, for example, RCP to elliptic polarizations are also validated likewise. The utilization of the normally ignored

copolarized spin light surely enhances the device performances and increases the functionalities. With the proper choice of materials and scaling of the designs, the method can be generalized to other wavelengths. This research extends and strengthens the practical applications of metasurfaces with phase and polarization manipulation.

5. Experimental Section

Numerical Simulations: The simulated material parameters of SiNx were adopted from the experimental measurement. The wavelength was fixed at $470\ \text{nm}$, and the refractive index was $n = 2.032094 + 0.000309i$. Full-wave simulations were conducted using commercial finite-difference time domain (FDTD) software, Lumerical. For individual nanopillars, perfectly matched layer (PML) conditions in the direction of the light propagation and periodic boundary conditions along all the in-plane directions were used. For the 3D metalens simulation, PML conditions were used in all the directions.

Fabrication of the Metasurfaces: The silicon nitride layer was deposited on the fused-silica substrate using the plasma enhanced chemical vapor deposition (PECVD) to a final thickness of $800\ \text{nm}$. Then, $200\ \text{nm}$ PMMA A4 resist film was spin coated onto the substrate and baked at 170°C for $5\ \text{min}$. Next, a $42\ \text{nm}$ thick layer of a water-soluble conductive polymer (AR-PC 5090) was spin coated on the resist for the dissipation of E-beam charges. The device pattern was written on an electron beam resist using E-beam writer (Elionix, ELS-F125). The conductive polymer was then dissolved in water and the resist was developed in a resist developer solution. An electron beam evaporated chromium layer was used to reverse the generated pattern with a liftoff process, and was then used as a hard mask for dry etching the silicon nitride layer. The dry etching was performed in a mixture of CHF₃ and SF₆ plasmas using an inductively coupled plasma reactive ion etching process (Oxford Instruments, PlasmaPro100 Cobra300). Finally, the chromium layer was removed by the stripping solution (ceric ammonium nitrate).

Optical Measurement: A white light laser (Fianium Super-continuum, $4\ \text{W}$) with a $470\ \text{nm}$ filter with a bandwidth of $10\ \text{nm}$ was used as the illumination source for holographic imaging and focus measurement. For the lens imaging, a halogen lamp was used for the illumination. A polarizer (Thorlabs, WP25L-VIS) and a QWP (Thorlabs, AQWP05M-600) were used

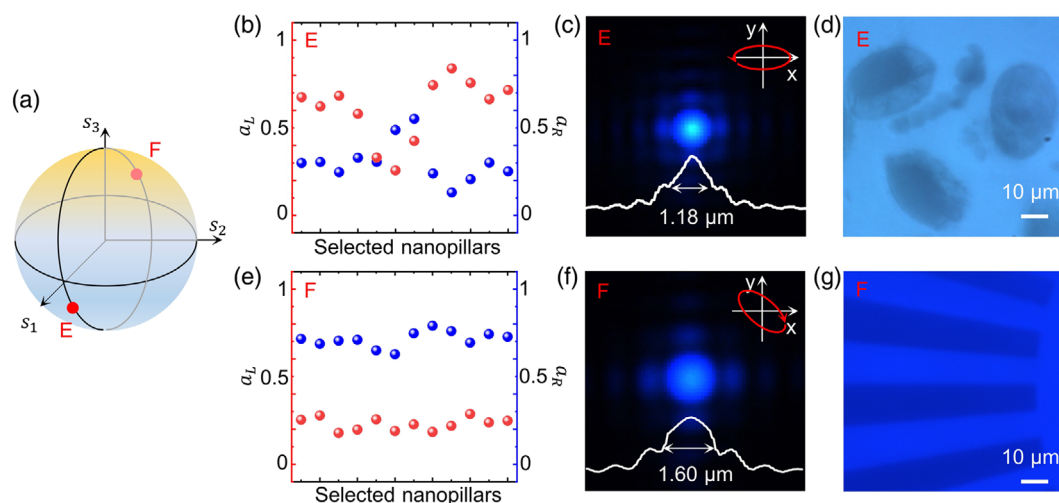


Figure 5. Realization of the metalens with elliptic polarization states. a) Red dots mark the designed elliptic polarization states on the Poincaré sphere. Amplitude distribution for the elliptic polarization state b) E and e) F. Intensity profile of the focus with the elliptic polarizations state c) E ($NA = 0.35$) and f) F ($NA = 0.24$). d) Direct image of the ascaris eggs with the metalens which has the elliptic polarization E focus. g) Direct image of the Sector Star Target with the metalens which has the elliptic polarization F focus.

for generating required polarization incidence and corresponding analyses, and an objective ($NA=0.9$, $100\times$) was used to collect the image.

Supporting Information

Supporting Information is available from the Wiley Online Library or from the author.

Acknowledgements

The authors acknowledge the microfabrication center of the National Laboratory of Solid State Microstructures (NLSSM) for technique support. This work was supported by the National Key R&D Program of China (2017YFA0303701, 2016YFA0202103), National Natural Science Foundation of China (Nos. 91850204, 11674167). T.L. thanks the support from Dengfeng Project B of Nanjing University.

Conflict of Interest

The authors declare no conflict of interest.

Keywords

geometric phase, metaholograms, metalens, propagation phase, quarter-wave plate

Received: November 20, 2020

Revised: December 7, 2020

Published online:

- [1] N. Yu, P. Genevet, M. A. Kats, F. Aieta, J.-P. Tetienne, F. Capasso, Z. Gaburro, *Science* **2011**, 334, 333.
- [2] H.-H. Hsiao, C. H. Chu, D. P. Tsai, *Small Methods* **2017**, 1, 1600064.
- [3] N. Yu, F. Capasso, *Nat. Mater.* **2014**, 13, 139.
- [4] S. M. Kamalia, E. Arbabi, A. Arbabi, A. Faraon, *Nanophotonics* **2018**, 7, 1041.
- [5] Z. Li, S. Yu, G. Zheng, *Nanophotonics* **2020**, 9, 3699.
- [6] Y. Hu, X. Wang, X. Luo, X. Ou, L. Li, Y. Chen, P. Yang, S. Wang, H. Duan, *Nanophotonics* **2020**, H.9, 3755.
- [7] S. Chen, W. Liu, Z. Li, H. Cheng, J. Tian, *Adv. Mater.* **2019**, 1805912.
- [8] M. Decker, I. Staude, M. Falkner, J. Dominguez, D. N. Neshev, I. Brener, T. Pertsch, Yuri S. Kivshar, *Adv. Optical Mater.* **2015**, 3, 813.
- [9] M. M. R. Elsayy, S. Lanteri, R. Duvigneau, J. A. Fan, P. Genevet, *Laser Photonics Rev.* **2020**, 14, 1900445.
- [10] Z. Li, W. Liu, H. Cheng, D.-Y. Choi, S. Chen, J. Tian, *Adv. Mater.* **2020**, 32, 1907983.
- [11] M. Khorasaninejad, F. Capasso, *Science* **2017**, 358, eaam8100.
- [12] M. Khorasaninejad, W. T. Chen, R. C. Devlin, J. Oh, A. Y. Zhu, F. Capasso, *Science* **2016**, 352, 1190.
- [13] H. Liang, A. Martins, B.-H. V. Borges, J. Zhou, E. R. Martins, J. Li, T. F. Krauss, *Optica* **2019**, 6, 1461.
- [14] C. Chen, W. Song, J.-W. Chen, J.-H. Wang, Y. H. Chen, B. Xu, M.-K. Chen, H. Li, B. Fang, J. Chen, H. Y. Kuo, S. Wang, D. P. Tsai, S. Zhu, T. Li, *Light: Sci. Appl.* **2019**, 8, 99.
- [15] M. Kang, Y. Ra'di, D. Farfan, A. Alù, *Phys. Rev. Appl.* **2020**, 13, 044016.
- [16] L. Huang, S. Zhang, T. Zentgraf, *Nanophotonics* **2018**, 7, 1169.
- [17] L. Wang, S. Kruk, H. Tang, T. Li, I. Kravchenko, D. N. Neshev, Y. S. Kivshar, *Optica* **2016**, 3, 1504.
- [18] G. Zheng, H. Mühlenbernd, M. Kenney, G. Li, T. Zentgraf, S. Zhang, *Nat. Nanotechnol.* **2015**, 10, 308.
- [19] P. C. Wu, W. Zhu, Z. X. Shen, P. H. J. Chong, W. Ser, D. P. Tsai, A.-Q. Liu, *Adv. Opt. Mater.* **2017**, 5, 1600938.
- [20] Z. Shi, A. Y. Zhu, Z. Li, Y.-W. Huang, W. T. Chen, C.-W. Qiu, F. Capasso, *Sci. Adv.* **2020**, 6, eaba3367.
- [21] P. C. Wu, W.-Y. Tsai, W. T. Chen, Y.-W. Huang, T.-Y. Chen, J.-W. Chen, C. Y. Liao, C. H. Chu, G. Sun, D. P. Tsai, *Nano Lett.* **2017**, 17, 445.
- [22] G. Li, M. Kang, S. Chen, S. Zhang, E. Y.-B. Pun, K. W. Cheah, J. Li, *Nano Lett.* **2013**, 13, 4148.
- [23] J. Li, S. Chen, H. Yang, J. Li, P. Yu, H. Cheng, C. Gu, H.-T. Chen, J. Tian, *Adv. Funct. Mater.* **2015**, 25, 704.
- [24] R. Zhao, B. Sain, Q. Wei, C. Tang, X. Li, T. Weiss, L. Huang, Y. Wang, T. Zentgraf, *Light Sci. Appl.* **2018**, 7, 95.
- [25] L. Yu, Y. Fan, Y. Wang, C. Zhang, W. Yang, Q. Song, S. Xiao, *Laser Photon. Rev.* **2020**, 14, 1900324.
- [26] Y. Yuan, K. Zhang, B. Ratni, Q. Song, X. Ding, Q. Wu, S. N. Burokur, P. Genevet, *Nat. Commun.* **2020**, 11, 4186.
- [27] Z.-L. Deng, J. Deng, X. Zhuang, S. Wang, K. Li, Y. Wang, Y. Chi, X. Ye, J. Xu, G. P. Wang, R. Zhao, X. Wang, Y. Cao, X. Cheng, G. Li, X. Li, *Nano Lett.* **2018**, 18, 2885.
- [28] Q. Song, A. Baroni, R. Sawant, P. Ni, V. Brandli, S. Chenot, S. Vézian, B. Damilano, P. D. Mierry, S. Khadir, P. Ferrand, P. Genevet, *Nat Commun.* **2020**, 11, 2651.
- [29] E. Arbabi, S. M. Kamali, A. Arbabi, A. Faraon, *ACS Photon.* **2019**, 6, 2712.
- [30] A. Arbabi, Y. Horie, M. Bagheri, A. Faraon, *Nat. Nanotechnol.* **2015**, 10, 937.
- [31] J. P. B. Mueller, N. A. Rubin, R. C. Devlin, B. Groever, F. Capasso, *Phys. Rev. Lett.* **2017**, 118, 113901.
- [32] Y. Guo, M. Pu, Z. Zhao, Y. Wang, J. Jin, P. Gao, X. Li, X. Ma, X. Luo, *ACS Photon.* **2016**, 3, 2022.
- [33] F. Zhang, M. Pu, J. Luo, H. Yu, X. Luo, *Opo-Elec Eng* **2017**, 44, 319.
- [34] Y. Yuan, K. Zhang, B. Ratni, Q. Song, X. Ding, Q. Wu, S. N. Burokur, P. Genevet, *Nat. Commun.* **2020**, 11, 4186.
- [35] K. Zhang, Y. Yuan, X. Ding, B. Ratni, S. N. Burokur, Q. Wu, *ACS Appl. Mater. Interfaces* **2019**, 11, 28423.
- [36] Y. Zhao, A. Alu, *Nano Lett.* **2013**, 13, 1086.
- [37] N. Yu, F. Aieta, P. Genevet, M. A. Kats, Z. Gaburro, F. Capasso, *Nano Lett.* **2012**, 12, 6328.
- [38] L. Huang, X. Chen, H. Mühlenbernd, G. Li, B. Bai, Qi. Tan, G. Jin, T. Zentgraf, S. Zhang, *Nano Lett.* **2012**, 12, 5750.
- [39] K. T. P. Lim, H. Liu, Y. Liu, J. K. W. Yang, *Nat. Commun.* **2019**, 10, 25.
- [40] W. T. Chen, K.-Y. Yang, C.-M. Wang, Y.-W. Huang, G. Sun, I.-D. Chiang, C. Y. Liao, W.-L. Hsu, H. T. Lin, S. Sun, L. Zhou, A. Q. Liu, D. P. Tsai, *Nano Lett.* **2014**, 14, 225.
- [41] S. M. Kamali, E. Arbabi, A. Arbabi, Y. Horie, A. Faraon, *Laser Photonics Rev.* **2016**, 10, 1002.
- [42] R. W. Gerchberg, W. O. Saxton, *Optik* **1972**, 35.
- [43] J. R. Fienup, *Appl. Opt.* **1982**, 21, 2758.
- [44] D. C. Chu, J. R. Fienup, *Opt. Eng.* **1974**, 13, 189.
- [45] F. Aieta, P. Genevet, M. A. Kats, N. Yu, R. Blanchard, Z. Gaburro, F. Capasso, *Nano Lett.* **2012**, 12, 4932.